An FCT finite element scheme for ideal MHD equations in 1d and 2d

M. Bittl[a], D. Kuzmin[a]

[a] *Institute of Applied Mathematics (LS III), TU Dortmund University, Vogelpothsweg 87, D-44227 Dortmund, Germany*

Abstract

We present a finite element (FE) scheme based on a flux-corrected transport (FCT) algorithm for solving the ideal MHD equations. The two main ingredients of the FCT scheme are the definition of a low-order scheme and the limiting strategy. For the low-order scheme we use an artificial viscosity operator based on scalar dissipation proportional to the fast wave speed. The accuracy of the low-order solution can be improved using a shock detector which allows to scale the amount of viscosity in such a way that a larger amount is used near discontinuities. The presented limiting strategy constrains the thermal pressure and the density leading to a synchronized correction factor for all conservative variables. For the 2d case we describe two predictor-corrector strategies for divergence cleaning where the FCT solution is used as predictor. The first follows the concept of unstaggered constrained transport where the magnetic vector potential is updated. The other strategy takes into account the concept of exact sequences and defines the divergence-free magnetic field in the Raviart-Thomas FE space. The proposed methods are applied to some standard test problems for ideal MHD to show their accuracy.

Keywords: ideal MHD equations, limiting, flux-corrected transport, finite elements, continuous Galerkin method

1. Introduction

The flux-corrected transport (FCT) technique was first introduced by Boris and Book [7] in the context of finite difference schemes for solving the transient continuity equation. The basic idea is to switch between a high-order method which can produce non-physical oscillations and a nonoscillatory, positivity preserving low-order method. Therefore, antidiffusive fluxes which define the difference between the low and high-order scheme are limited in such a way that no unphysical extrema occur. If no limiting is done, the high-order scheme is

Email addresses: melanie.bittl@math.tu-dortmund.de (M. Bittl), kuzmin@math.uni-dortmund.de (D. Kuzmin)

obtained, whereas the low-order scheme is obtained if all antidiffusive fluxes are canceled. Besides hydrodynamic problems [6, 28] also magnetohydrodynamic (MHD) problems [11, 27] have been considered in the context of FCT finite difference schemes. As with other methods considering MHD equations the main difficulty is to keep the magnetic field divergence-free [8, 26]. Tóth [27] used Powell's [21] corrective terms, i.e. terms proportional to $\nabla \cdot \mathbf{B}$, to stabilize the FCT solution. DeVore [11] used staggered grids and divided the antidiffusive fluxes into components which are limited independently.

FCT for the finite element method was first considerd in [20] for scalar advection. Further extensions to the Euler and Navier-Stokes equations can be found e.g. in [17, 18, 14, 15]. The high-order scheme is given by the standard Galerkin finite element method. To derive the low-order scheme an artificial viscosity operator is added and the consistent mass matrix of the fully discrete scheme is replaced by its lumped counterpart. In the case of a single equation the limiting can be directly performed by Zalesak's algorithm [28]. Considering a system of equations there are different strategies for the limiting process (see e.g. [14]). The probably most popular approach is to synchronize the correction factors of the antidiffusive fluxes for all conservative variables, where the individual correction factors can be calculated by Zalesak's algorithm.

In this paper we will extend the FEM-FCT scheme for the Euler equations [14] to MHD equations. Therefore we will first describe a predictor-corrector FCT approach and present an artificial viscosity operator leading to scalar dissipation proportional to the fast wave speed. This viscosity operator can be scaled using a shock detector which allows to use the full amount of diffusion near discontinuities and less in cells where the solution is smooth or constant. The limiting strategy is adopted from [16] and constrains the density and the thermal pressure in a synchronized way. This already leads to a usable MHD algorithm in 1d. In 2d we have to add an additional step for divergence cleaning. Here we consider two approaches: the first follows the unstaggered constrained transport (CT) algorithm of [22], where the magnetic potential $\mathbf{A}$ has to be updated in each step such that the magnetic field can be calculated by $\mathbf{B} = \nabla \times \mathbf{A}$. The second approach takes into account FE spaces forming exact sequences within the framework of the discrete de Rham complex [5] and defines the magnetic field in the Raviart-Thomas FE space.

We perform some 1d experiments to compare the numerical solutions calculated by scaled and not scaled artificial viscosity operators. In 2d we compare the numerical results of both divergence cleaning schemes. All examples show that rarefaction waves, shocks and contact discontinuities are resolved very well.

2. Element-based FEM-FCT scheme for MHD

The system of ideal MHD equations can be written in generic divergence form

$$\frac{\partial U}{\partial t} + \nabla \cdot \mathbf{F} = 0. \tag{1}$$

The conservative variables U and the fluxes $\mathbf{F}$ are given by

$$U = \begin{bmatrix} \rho \\ \rho\mathbf{u} \\ \rho e \\ \mathbf{B} \end{bmatrix}, \quad \mathbf{F} = \begin{bmatrix} \rho\mathbf{u} \\ \rho\mathbf{u} \otimes \mathbf{u} + p_{tot} I - \mathbf{B} \otimes \mathbf{B} \\ \rho e\mathbf{u} + p_{tot}\mathbf{u} - \mathbf{B}(\mathbf{u} \cdot \mathbf{B}) \\ \mathbf{u} \otimes \mathbf{B} - \mathbf{B} \otimes \mathbf{u} \end{bmatrix}, \tag{2}$$

where ρ is the density, $\mathbf{u} = (u_x, u_y, u_z)$ is the velocity, ρe is the total energy and $\mathbf{B} = (B_x, B_y, B_z)$ is the magnetic field. The total pressure p_{tot} is given by the sum of thermal and magnetic pressures

$$p_{tot} = p + \frac{1}{2}|\mathbf{B}|^2. \tag{3}$$

The thermal pressure p is defined by the equation of state

$$p = (\gamma - 1)\left(\rho e - \frac{\rho|\mathbf{u}|^2}{2} - \frac{1}{2}|\mathbf{B}|^2\right), \tag{4}$$

where γ is the adiabatic constant depending on the physical properties of the fluid. We use the group finite element formulation [12] to approximate U and $\mathbf{F}$

$$U_h = \sum_j U_j \varphi_j, \quad \mathbf{F}_h = \sum_j \mathbf{F}_j \varphi_j, \tag{5}$$

where φ_i are continuous basis functions associated with the space of linear finite elements. Substituting these approximations into the Galerkin variational form of the MHD system, integrating by parts and using the Crank-Nicolson scheme to discretize in time, we obtain the fully discrete problem

$$\underbrace{\frac{1}{\Delta t} M_C \left(U^{n+1} - U^n\right) - \frac{1}{2}\left[K(U^{n+1}) + K(U^n)\right] - S(U^n)}_{=:G_H(U^{n+1})} = 0, \tag{6}$$

where M_C is the consistent mass matrix, $K(U)$ is the vector of volume integrals associated with the discretization of $\nabla\cdot\mathbf{F}$ and $S(U)$ is the vector of corresponding surface integrals. When it comes to enforcing discrete maximum principles within the framework of algebraic flux correction [13, 14], the discrete problem (6) is decomposed into a monotone low-order part and an antidiffusive term. Introducing the lumped mass matrix M_L and an artificial viscosity operator $D(U)$, which will be defined later, we obtain the equivalent representation

$$\underbrace{\frac{M_L}{\Delta t}\left(U^{n+1} - U^n\right) - L(U^{n+1}) - S(U^n)}_{=:G_L(U^{n+1})} - F(U^{n+1}, U^n) = 0 \tag{7}$$

where $L(U) := K(U) + D(U)U$ is the nonoscillatory part of $K(U)$ and

$$F(U^{n+1}, U^n) := \frac{1}{\Delta t}(M_L - M_C)\left(U^{n+1} - U^n\right) + \frac{1}{2}\left[K(U^{n+1}) + K(U^n)\right] - L(U^{n+1}) \tag{8}$$

is the antidiffusive term assembled from massless element contributions

$$F_i(U^{n+1}, U^n) = \sum_{el} F_{el,i}, \quad \sum_i F_{el,i} = 0. \tag{9}$$

To enforce monotonicity constraints, each element vector F_{el} is multiplied by a solution-dependent correction factor α_{el}. The details of the limiting procedure will be provided later.

Our predictor-corrector FCT approach to solving the ideal MHD equations is as follows:

1. Calculate the solution U_L of the low-order nonlinear system

$$G_L(U_L) = 0. \tag{10}$$

2. Assemble the limited antidiffusive term $\bar{F}(U_L, U^n)$ and correct the low-order approximation

$$U^{n+1} = U_L + \Delta t M_L^{-1} \bar{F}(U_L, U^n). \tag{11}$$

The accuracy of the constrained Galerkin solution U^{n+1} depends on the definition of the artificial viscosity operator $D(U)$ and on the algorithm for calculating the correction factors for the limited antidiffusive contributions presented in the following.

2.1. Artificial viscosity operator

In this paper we make use of an artificial viscosity operator based on Rusanov-like scalar dissipation. This approach has been successfully applied to the compressible Euler equations [14, 15] and is now extended to the ideal MHD equations.

The artificial viscosity operator based on scalar dissipation is given by

$$D_{ij}^{fast}(U) = max\{d_{ij}, d_{ji}\} I, \quad \forall i \neq j, \tag{12}$$

$$D_{ii}^{fast}(U) = -\sum_{j \neq i} D_{ij}(U). \tag{13}$$

The scalar-valued artificial diffusion coefficients d_{ij} are defined by

$$d_{ij} = |\mathbf{g}_{ij} \cdot \mathbf{u}_j| + |\mathbf{g}_{ij} \cdot \mathbf{c}_j^f|, \quad \forall i \neq j \tag{14}$$

$$\mathbf{g}_{ij} := \frac{1}{2}(\mathbf{c}_{ji} - \mathbf{c}_{ij}), \quad \mathbf{c}_{ij} = \int_\Omega \varphi_i \nabla \varphi_j, \tag{15}$$

$$\mathbf{c}_j^f = (c_f(\mathbf{e}_1, U_j), ..., c_f(\mathbf{e}_{dim}, U_j))^T, \tag{16}$$

$$a = a(U) = \sqrt{\frac{\gamma p}{\rho}}, \quad c_a = c_a(\mathbf{e}, U) = \sqrt{\frac{(\mathbf{B} \cdot \mathbf{e})^2}{\rho}}, \tag{17}$$

$$c_f(\mathbf{e}, U) = \left\{ \frac{1}{2} \left[a^2 + \frac{|\mathbf{B}|^2}{\rho} + \sqrt{\left(a^2 + \frac{|\mathbf{B}|^2}{\rho} \right)^2 - 4a^2 c_a^2} \right] \right\}^{0.5}, \tag{18}$$

where $\{\mathbf{e}_i\}_{i=1}^{dim}$ is the set of unit vectors. This leads to dissipation proportional to the fast wave speed.

To improve the accuracy of the low-order scheme we scale the artificial viscosity operator in such a way that the full amount is used near discontinuities whereas less diffusion is applied in regions where the solution is smooth or constant. Therefore we make use of the following shock detector [3]

$$\mu_i^u := \begin{cases} \frac{|\sum_{j\in S(i)} u_i - u_j|}{\sum_{j\in S(i)} |u_i - u_j|} & \text{if } \sum_{j\in S(i)} |u_i - u_j| \neq 0, \\ 0 & \text{otherwise,} \end{cases} \tag{19}$$

where u_i is the nodal value of the quantity u evaluated at node x_i and $S(i)$ is the set of nearest neighbors of node i. This detector can be used to scale the coefficients d_{ij} of our artificial viscosity operator in the following way

$$d_{ij}^{\rho,\rho\mathbf{u},\rho e} = \mu_i^{\rho} |\mathbf{g}_{ij} \cdot \mathbf{u}_j| + \mu_i^{p} |\mathbf{g}_{ij} \cdot \mathbf{c}_j^f|, \quad \forall i \neq j \tag{20}$$

$$d_{ij}^{\mathbf{B}} = \mu^{\mathbf{B}} \left(|\mathbf{g}_{ij} \cdot \mathbf{u}_j| + |\mathbf{g}_{ij} \cdot \mathbf{c}_j^f| \right), \quad \forall i \neq j \tag{21}$$

where $\mu^{\mathbf{B}} = \max\{\mu^{B_x}, \mu^{B_y}, \mu^{B_z}\}$.

For implementation purposes we replace the condition $\sum_{j\in S(i)} |u_i - u_j| \neq 0$ in (19) by $\sum_{j\in S(i)} |u_i - u_j| > \frac{\epsilon |u_i|}{\#DOFs}$, where $\epsilon > 0$ is a small parameter (in our computations $\epsilon = 10^{-4}$).

2.2. Limiting strategy

At the corrector step of the FCT scheme, the element contributions F_{el} to the antidiffusive term

$$F_i(U_L, U^n) = (f_i^{\rho}, \boldsymbol{f}_i^{\rho\mathbf{u}}, f_i^{\rho e}, \boldsymbol{f}_i^{\mathbf{B}})^T \tag{22}$$

are limited in such a way that no over- or undershoots can occur in the quantities of interest. Using the same correction factor α_{el} for all variables, we obtain the limited antidiffusive correction

$$\bar{F}_i(U_L, U^n) = \sum_{el} \alpha_{el} F_{el,i}. \tag{23}$$

Adopting the methodology developed in [16] in the context of synchronized FCT limiting for the Euler equations, we first calculate provisional correction factors α_{el}^{ρ} to constrain the density ρ and then calculate correction factors α_{el}^{p} constraining the thermal pressure p. The synchronized correction factors are then given by $\alpha_{el} := \alpha_{el}^{\rho} \alpha_{el}^{p}$.

The density limiter. The density should be constrained in such a way that

$$\rho_i^{\min} \le \rho_i = \rho_i^L + \frac{1}{m_i}\sum_{el} \alpha_{el} f_{el,i}^{\rho} \le \rho_i^{\max} \tag{24}$$

where m_i is the entry of the lumped mass matrix multiplied by $\frac{1}{\Delta t}$. The bounds $\rho_i^{\min}$ and $\rho_i^{\max}$ are defined by

$$\rho_i^{\min} := \min_{j\in N(i)} \rho_j^L, \quad \rho_i^{\max} := \max_{j\in N(i)} \rho_j^L, \tag{25}$$

where $N(i) = S(i)\cup\{i\}$ is the set of nodes containing i and its nearest neighbors $j \neq i$.

The calculation of the correction factors α_{el}^{ρ} is based on Zalesak's limiter [28] and involves the following steps:

1. Compute the sums of positive/negative element fluxes

$$P_i^+ = \sum_{el} \max\{0, f_{el,i}^{\rho}\}, \qquad P_i^- = \sum_{el} \min\{0, f_{el,i}^{\rho}\}. \tag{26}$$

2. Compute the distance to local maximum/minimum of the low-order approximation

$$Q_i^+ = \frac{m_i}{\Delta t}(\rho_i^{\max} - \rho_i^L), \qquad Q_i^- = \frac{m_i}{\Delta t}(\rho_i^{\min} - \rho_i^L). \tag{27}$$

3. Compute the element-based correction factors α_{el}^{ρ} for the density ρ

$$R_i^{\pm} = \min\{1, \frac{Q_i^{\pm}}{P_i^{\pm}}\}, \quad \alpha_{el,i}^{\rho} = \begin{cases} R_i^+ & \text{if } f_{el,i}^{\rho} > 0, \\ 1 & \text{if } f_{el,i}^{\rho} = 0, \\ R_i^- & \text{if } f_{el,i}^{\rho} < 0, \end{cases} \tag{28}$$

$$\alpha_{el}^{\rho} = \min_{i\in el} \alpha_{el,i}^{\rho}. \tag{29}$$

These first provisional correction factors α_{el}^{ρ} are now used to define the tight density bounds

$$\tilde{\rho}_i^{\max} = \rho_i^L + \frac{1}{m_i}\sum_{el} \max\{0, \alpha_{el}^{\rho} f_{el,i}^{\rho}\}, \tag{30}$$

$$\tilde{\rho}_i^{\min} = \rho_i^L + \frac{1}{m_i}\sum_{el} \min\{0, \alpha_{el}^{\rho} f_{el,i}^{\rho}\}, \tag{31}$$

which we need in the definition of the bounds for the pressure (see below). Note that $\tilde{\rho}_i^{\min}$ is nonnegative due to the definition of α_{el}^{ρ}.

The pressure limiter. To constrain the thermal pressure we define the local bounds for p_i as

$$\tilde{\rho}_i^{\min} p_i^{\min} \leq \rho_i p_i = \rho_i(\gamma-1)\left((\rho e)_i - \frac{|(\rho\mathbf{u})_i|^2}{2\rho_i} - \frac{1}{2}|\mathbf{B}_i|^2\right) \leq \tilde{\rho}_i^{\max} p_i^{\max}, \quad (32)$$

$$p_i^{\min} = \min_{j\in N(i)} (\gamma-1)\left((\rho e)_j^L - \frac{\left|(\rho\mathbf{u})_j^L\right|^2}{2\rho_j^L} - \frac{1}{2}|\mathbf{B}_j^L|^2\right), \quad (33)$$

$$p_i^{\max} = \max_{j\in N(i)} (\gamma-1)\left((\rho e)_j^L - \frac{\left|(\rho\mathbf{u})_j^L\right|^2}{2\rho_j^L} - \frac{1}{2}|\mathbf{B}_j^L|^2\right). \quad (34)$$

Note that if we would constrain p_i such that $p_i^{\min} \leq p_i \leq p_i^{\max}$, the limiter would cancel all antidiffusive fluxes in the regions of constant pressure. In the presence of a contact discontinuity in the density, this would strongly smear out the discontinuity due to the synchronized limiting. For this reason the pressure constraint (32) is preferred.

The constrained pressure p_i depends on the synchronized correction factors $\alpha_{el} \leq \alpha_{el}^{\rho}$ and conservatives fluxes $(f_{el,i}^{\rho}, \boldsymbol{f}_{el,i}^{\rho\mathbf{u}}, f_{el,i}^{\rho e}, \boldsymbol{f}_{el,i}^{\mathbf{B}})$ as follows:

$$\begin{aligned}
\frac{\rho_i p_i}{(\gamma-1)} &= \left(\rho_i^L + \frac{1}{m_i}\sum_{el}\alpha_{el} f_{el,i}^{\rho}\right)\left((\rho e)_i^L + \frac{1}{m_i}\sum_{el}\alpha_{el} f_{el,i}^{\rho e}\right) \\
&\quad - \frac{1}{2}\left((\rho\mathbf{u})_i^L + \frac{1}{m_i}\sum_{el}\alpha_{el} f_{el,i}^{\rho\mathbf{u}}\right)^2 \\
&\quad - \frac{1}{2}\left(\rho_i^L + \frac{1}{m_i}\sum_{el}\alpha_{el} f_{el,i}^{\rho}\right)\left(\mathbf{B}_i^L + \frac{1}{m_i}\sum_{el}\alpha_{el} f_{el,i}^{\mathbf{B}}\right)^2 \\
&= \frac{\rho_i^L p_i^L}{(\gamma-1)} + \frac{1}{m_i}\sum_{el}\alpha_{el}\left(\rho_i^L f_{el,i}^{\rho e} + (\rho e)_i^L f_{el,i}^{\rho} - (\rho\mathbf{u})_i^L \cdot f_{el,i}^{\rho\mathbf{u}} - \frac{1}{2}\left|\mathbf{B}_i^L\right|^2 f_{el,i}^{\rho} - \rho_i^L \mathbf{B}_i^L \cdot f_{el,i}^{\mathbf{B}}\right) \\
&\quad + \left(\frac{1}{m_i}\sum_{el}\alpha_{el} f_{el,i}^{\rho}\right)\left(\frac{1}{m_i}\sum_{el}\alpha_{el} f_{el,i}^{\rho e}\right) - \frac{1}{2}\left|\frac{1}{m_i}\sum_{el}\alpha_{el} f_{el,i}^{\rho\mathbf{u}}\right|^2 \\
&\quad - \frac{1}{2}\rho_i^L\left|\frac{1}{m_i}\sum_{el}\alpha_{el} f_{el,i}^{\mathbf{B}}\right|^2 - \left(\frac{1}{m_i}\sum_{el}\alpha_{el} f_{el,i}^{\rho}\right)\left(\frac{1}{m_i}\sum_{el}\alpha_{el}\mathbf{B}_i^L \cdot f_{el,i}^{\mathbf{B}}\right) \\
&\quad - \frac{1}{2}\left(\frac{1}{m_i}\sum_{el}\alpha_{el} f_{el,i}^{\rho}\right)\left|\frac{1}{m_i}\sum_{el}\alpha_{el} f_{el,i}^{\mathbf{B}}\right|^2. \quad (35)
\end{aligned}$$

Considering the worst-case scenario we obtain the following estimates

$$\frac{m_i^2 Q_i^{-,p}}{(\gamma-1)} \leq R_i^{-,p} P_i^{-,p} \leq \frac{m_i^2\left(\rho_i p_i - \rho_i^L p_i^L\right)}{(\gamma-1)} \leq R_i^{+,p} P_i^{+,p} \leq \frac{m_i^2 Q_i^{+,p}}{(\gamma-1)}, \quad (36)$$

where

$$P_i^{+,p} = m_i \sum_{el} \max\left\{0, \alpha_{el}^{\rho}\left(\rho_i^L f_{el,i}^{\rho e} + (\rho e)_i^L f_{el,i}^{\rho} - (\rho \mathbf{u})_i^L \cdot f_{el,i}^{\rho \mathbf{u}} - \frac{1}{2}\left|\mathbf{B}_i^L\right|^2 f_{el,i}^{\rho} - \rho_i^L \mathbf{B}_i^L \cdot f_{el,i}^{\mathbf{B}}\right)\right\}$$
$$+ \sum_{el1}\sum_{el2} \max\left\{0, \alpha_{el1}^{\rho} f_{el1,i}^{\rho} \alpha_{el2}^{\rho} f_{el2,i}^{\rho e}\right\} + \sum_{el1}\sum_{el2} \max\left\{0, -\alpha_{el1}^{\rho} f_{el1,i}^{\rho} \alpha_{el2}^{\rho} \mathbf{B}_i^L \cdot f_{el2,i}^{\mathbf{B}}\right\}$$
$$+ \frac{1}{2m_i} \sum_{el1} \max\left\{0, -\alpha_{el1}^{\rho} f_{el1,i}^{\rho} \left|\sum_{el2} \alpha_{el2}^{\rho} f_{el2,i}^{\mathbf{B}}\right|^2\right\} \tag{37}$$

$$P_i^{-,p} = m_i \sum_{el} \min\left\{0, \alpha_{el}^{\rho}\left(\rho_i^L f_{el,i}^{\rho e} + (\rho e)_i^L f_{el,i}^{\rho} - (\rho \mathbf{u})_i^L \cdot f_{el,i}^{\rho \mathbf{u}} - \frac{1}{2}\left|\mathbf{B}_i^L\right|^2 f_{el,i}^{\rho} - \rho_i^L \mathbf{B}_i^L \cdot f_{el,i}^{\mathbf{B}}\right)\right\}$$
$$+ \sum_{el1}\sum_{el2} \min\left\{0, \alpha_{el1}^{\rho} f_{el1,i}^{\rho} \alpha_{el2}^{\rho} f_{el2,i}^{\rho e}\right\} - \frac{1}{2}\left(\sum_{el} \alpha_{el}^{\rho} \left|f_{el,i}^{\rho \mathbf{u}}\right|\right)^2 - \frac{1}{2}\rho_i^L \left(\sum_{el} \alpha_{el}^{\rho} \left|f_{el,i}^{\mathbf{B}}\right|\right)^2$$
$$+ \sum_{el1}\sum_{el2} \min\left\{0, -\alpha_{el1}^{\rho} f_{el1,i}^{\rho} \alpha_{el2}^{\rho} \mathbf{B}_i^L \cdot f_{el2,i}^{\mathbf{B}}\right\} + \frac{1}{2m_i} \sum_{el1} \min\left\{0, -\alpha_{el1}^{\rho} f_{el1,i}^{\rho} \left|\sum_{el2} \alpha_{el2}^{\rho} f_{el2,i}^{\mathbf{B}}\right|^2\right\} \tag{38}$$

$$Q_i^{+,p} = \tilde{\rho}_i^{\max} p_i^{\max} - \rho_i^L p_i^L, \quad Q_i^{-,p} = \tilde{\rho}_i^{\min} p_i^{\min} - \rho_i^L p_i^L, \tag{39}$$

$$R_i^{+,p} = \min\left\{1, \frac{m_i^2 Q_i^{+,p}}{P_i^{+,p}(\gamma - 1)}\right\}, \quad R_i^{-,p} = \min\left\{1, \frac{m_i^2 Q_i^{-,p}}{P_i^{-,p}(\gamma - 1)}\right\}. \tag{40}$$

The correction factor α_{el}^p is then given by

$$\alpha_{el}^p = \min_{i \in el} \alpha_{el,i}^p, \quad \alpha_{el,i}^p = \min\{R_i^{+,p}, R_i^{-,p}\}. \tag{41}$$

This yields the synchronized correction factor

$$\alpha_{el} = \alpha_{el}^p \alpha_{el}^{\rho}. \tag{42}$$

3. Divergence cleaning

The equation for the magnetic field $\mathbf{B}$

$$\frac{\partial \mathbf{B}}{\partial t} + \nabla \cdot (\mathbf{u} \otimes \mathbf{B} - \mathbf{B} \otimes \mathbf{u}) = 0, \tag{43}$$

can be written in an equivalent form

$$\frac{\partial \mathbf{B}}{\partial t} + \nabla \times (\mathbf{B} \times \mathbf{u}) = 0. \tag{44}$$

Taking the divergence of this equation and assuming that the initial magnetic field is divergence-free, we obtain

$$\nabla \cdot \mathbf{B} = 0. \tag{45}$$

Numerical schemes which do not satisfy this "constraint" may give rise to instabilities and nonphysical solutions [8]. Note that this constraint implies that B_x is constant in 1d. Therefore, the following divergence cleaning techniques are only necessary for the 2d case.

In this paper we follow the approach of divergence cleaning based on the unstaggered constrained transport (CT) algorithm introduced by Rossmanith [22] in the context of a discontinuous Galerkin (DG) method. We have

$$\mathbf{B} = \nabla \times \mathbf{A}, \tag{46}$$

where $\mathbf{A}$ is the magnetic vector potential satisfying the weakly hyperbolic transport equation

$$\frac{\partial \mathbf{A}}{\partial t} + \mathbf{B} \times \mathbf{u} = 0. \tag{47}$$

The unstaggered CT approach to divergence cleaning leads to the following correction procedure:

1. Use the FCT predictor $\mathbf{B}^\star$ to update the nodal magnetic potentials

$$\mathbf{A}_i^{n+1} = \mathbf{A}_i^n - \Delta t(\mathbf{B}_i^\star \times \mathbf{u}_i^{n+1}). \tag{48}$$

2. Overwrite $\mathbf{B}^\star$ by the (constrained) L^2 projection of $\nabla \times \mathbf{A}_h^{n+1}$ into the nodal $P1$ space

$$\mathbf{B}^{n+1} = PC\mathbf{A}^{n+1} \tag{49}$$

where C is the discrete curl operator and P is the operator associated with the L^2 projection into the continuous linear finite element space.

Another approach we would like to present here takes into account finite element spaces forming exact sequences within the framework of the discrete de Rham complex [5]. Therefore, we consider the electric field

$$\mathbf{E} = \mathbf{B} \times \mathbf{u}, \quad \mathbf{E} = (E_1, E_2, E_3) \tag{50}$$

and write equation (44) as

$$\frac{\partial \mathbf{B}}{\partial t} + \nabla \times \mathbf{E} = 0, \tag{51}$$

where $\mathbf{E} \in H(\mathbf{curl})$ and $\mathbf{B} \in H(div)$. In 3d those spaces can be discretized using Nédélec and Raviart-Thomas elements. In 2d we only have to consider the first two components of $\mathbf{B}$ and therefore, equation (51) can be written as

$$\frac{\partial B_x}{\partial t} + \frac{\partial E_3}{\partial y} = 0, \tag{52}$$

$$\frac{\partial B_y}{\partial t} - \frac{\partial E_3}{\partial x} = 0, \tag{53}$$

where $E_3 = B_x u_y - B_y u_x$. Using the 2d definition of the **curl** operator

$$\mathbf{curl} E_3 = (\frac{\partial E_3}{\partial y}, -\frac{\partial E_3}{\partial x})^T, \tag{54}$$

we have $E_3 \in H(\mathbf{curl})$ and $(B_x, B_y)^T \in H(div)$. For the discretization of those spaces we use the continuous Lagrange finite element space and the Raviart-Thomas finite element in 2d which form an exact sequence (see, e.g. [1, 10]). This yields the following steps for divergence cleaning:

1. Use the FCT predictor $\mathbf{B}^\star$ to obtain

$$E_3 = P(\mathbf{B}^\star \times \mathbf{u}^{n+1}). \tag{55}$$

2. Update the reduced magnetic field $\mathbf{B}_{RT} = (B_x, B_y)$ of the Raviart-Thomas finite element space

$$\mathbf{B}_{RT}^{n+1} = \mathbf{B}_{RT}^n - \Delta t \mathbf{curl} E_3. \tag{56}$$

3. Overwrite $(B_x^\star, B_y^\star)$ by the L^2 projection of $\mathbf{B}_{RT}^{n+1}$ into the nodal $P1$ space

$$(B_x^{n+1}, B_y^{n+1})^T = P\mathbf{B}_{RT}^{n+1}. \tag{57}$$

Since the divergence of a curl is identically zero, we obtain a divergence-free (in the weak sense) magnetic field $\mathbf{B}_{RT}^{n+1}$ if $\mathbf{B}_{RT}^n$ is divergence-free in the weak sense.

In the following we will refer to the first approach as "potA" approach and the second as "RT" approach.

4. Numerical results

In this section we will present numerical results for 1d and 2d test problems. The algorithms described above are implemented using the software of the FEniCS project [2]. In the case that we do not have an exact solution of our test problem, we will compare our results with those obtained by the Athena project [25], which uses CT algorithms in the context of a finite volume method.

4.1. 1d Brio-Wu problem

At first we consider the Brio-Wu shock tube problem [9] which is an extension of Sod's shock tube problem [24] to MHD. The initial data is given by

$$\begin{aligned}(\rho, u_x, u_y, u_z, p, B_y, B_z)^{left} &= (1.0, 0, 0.0, 0., 1, 1, 0),\\ (\rho, u_x, u_y, u_z, p, B_y, B_z)^{right} &= (0.125, 0, 0.0, 0., 0.1, -1, 0),\end{aligned} \tag{58}$$

and $B_x = 0.75$, $\gamma = 2.$.

In Fig. 1 the numerical solutions computed by the FCT scheme and the low-order scheme (10) with and without the shock detector scaling ('$+\mu$') are shown. The reference solution is computed by the Athena code [25] on a grid with 100,000 zones. Looking at the density from the left to the right we have

a rarefaction wave, a compound wave, a contact discontinuity, a shock, and a rarefaction wave. In the first and third row, we see that the low-order solution computed with the μ-scaled artificial viscosity operator (20) is more accurate than without that scaling. The FCT solutions are shown in the other rows and are more accurate than the low-order solutions. Comparing the FCT solutions computed with and without the shock detector scaling we see that those do not much differ from each other. However, the use of the μ-scaled artificial viscosity operator eliminates the spurious kink in Fig. 1(i).

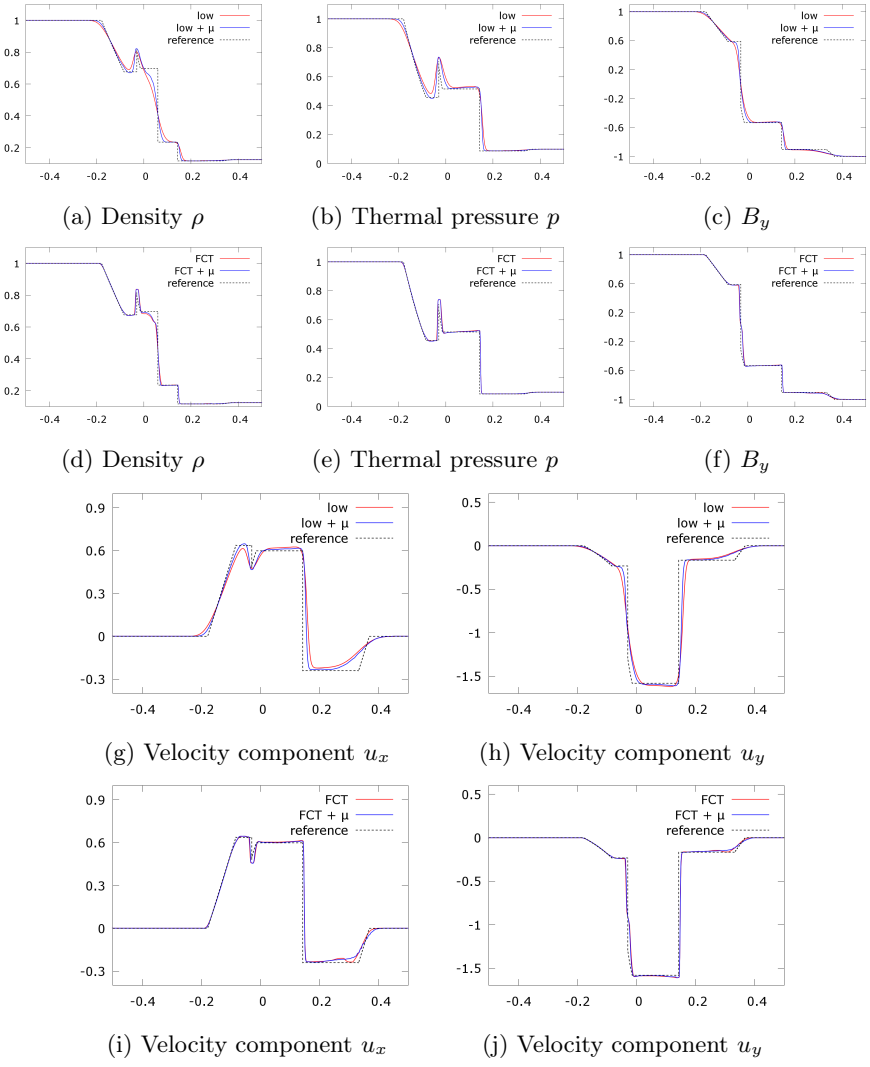

(a) Density ρ (b) Thermal pressure p (c) B_y

(d) Density ρ (e) Thermal pressure p (f) B_y

(g) Velocity component u_x (h) Velocity component u_y

(i) Velocity component u_x (j) Velocity component u_y

Figure 1: Numerical solutions of the Brio-Wu problem using the viscosity operator (14) and its scaled version "+μ" (20) at $T_{end} = 0.1$ ($h = \frac{1}{512}$)

4.2. 1d Ryu-Jones problem

In this test case we consider the Riemann problem "2a" from [23]. The initial data is given by

$$(\rho, u_x, u_y, u_z, p, B_y, B_z)^{left} = (1.08, 1.2, 0.01, 0.5, 0.95, \frac{3.6}{\sqrt{4\pi}}, \frac{2}{\sqrt{4\pi}}),$$
$$(\rho, u_x, u_y, u_z, p, B_y, B_z)^{right} = (1.0, 0, 0., 0., 1., \frac{4}{\sqrt{4\pi}}, \frac{2}{\sqrt{4\pi}}), \tag{59}$$

and $B_x = \frac{2}{\sqrt{4\pi}}$, $\gamma = \frac{5}{3}$. The solution consists of a contact discontinuity from which fast shocks, rotational discontinuities and slow shocks propagate.

In Figures 2 and 3 we show the numerical solutions computed by the FCT scheme and the low-order scheme. The first and the third row of Fig. 2 and the first row of Fig. 3 show the low-order solutions, whereas in the other rows the solutions computed by the FCT scheme are displayed. As before we see that the low-order solution computed with the μ-scaled artificial viscosity operator is more accurate than the not-scaled version. The FCT solutions are again more accurate than the low-order solutions. We see here also that the scaled version of the viscosity operator leads to a more accurate FCT solution, which can be seen very well in the density and pressure component.

If we have a look at the third component of the magnetic or velocity field, we see that the regions of rotational discontinuities are strongly smeared. The reason for that behaviour lies mainly in our limiting strategy. We only constrain the density and the thermal pressure and therefore, in regions where those are constant the antidiffusive fluxes are canceled and the values of the low-order solution are adopted. If the low-order solution would resolve the rotational discontinuities (e.g. by using a finer grid), the FCT solution would be less smeared in those regions.

Table 1 presents the L^1 error for the numerical solutions and the experimental order of convergence (EOC) defined by $EOC = \log_2\left(\frac{\|u-u_{2h}\|_{L^1}}{\|u-u_h\|_{L^1}}\right)$. It can be seen that using the μ-scaled artificial viscosity operator yields higher accuracy than the not-scaled operator. The EOC varies between 0.48 and 0.8 which are reasonable orders for discontinuous solutions.

	FCT		FCT + μ	
h	L^1 error	EOC	L^1 error	EOC
1/128	0.11655	-	0.0985344	-
1/256	0.0713027	0.71	0.0566824	0.80
1/512	0.0444526	0.68	0.0328456	0.79
1/1024	0.0293975	0.60	0.0213667	0.62
1/2048	0.018919	0.64	0.014432	0.57
1/4096	0.0131282	0.53	0.0103488	0.48

Table 1: L^1 error for the Ryu-Jones problem

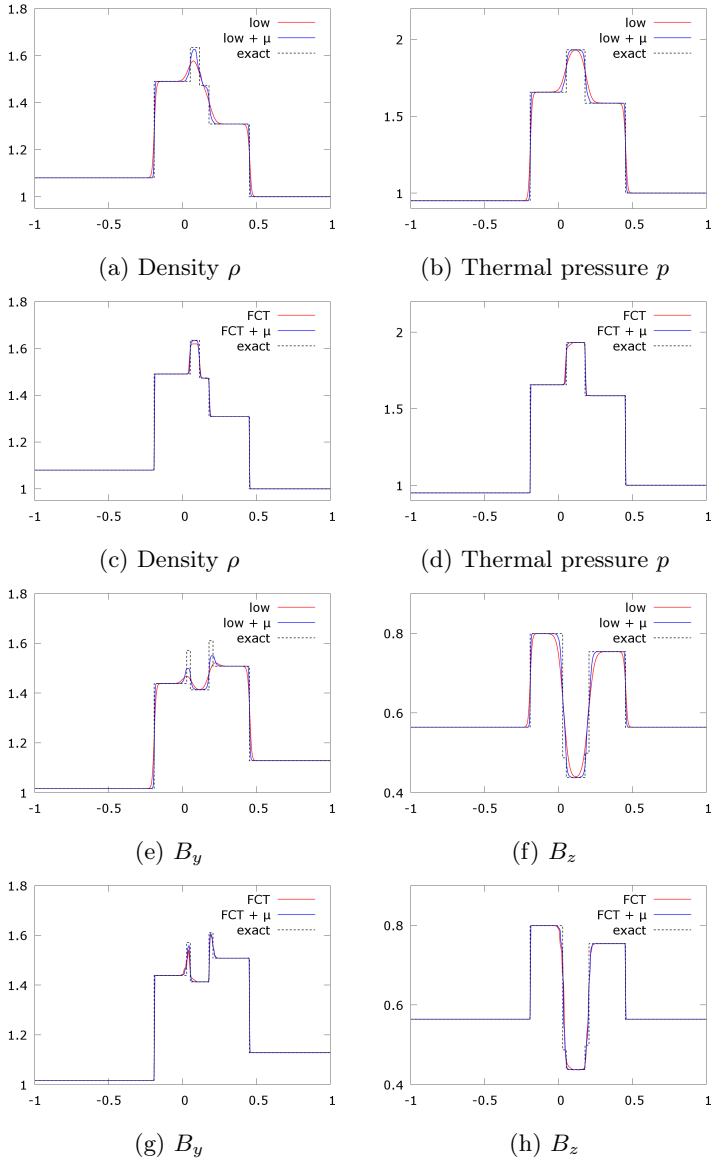

(a) Density ρ (b) Thermal pressure p

(c) Density ρ (d) Thermal pressure p

(e) B_y (f) B_z

(g) B_y (h) B_z

Figure 2: Numerical solutions of the Ryu-Jones problem using the viscosity operator (14) and its scaled version "$+\mu$" (20) at $T_{end} = 0.2$ ($h = \frac{1}{512}$)

4.3. 2d - rotor problem

The first 2d problem is a variation of the well known rotor problem [4, 26]. The domain is a unit square $(0, 1) \times (0, 1)$ and we will use the following initial

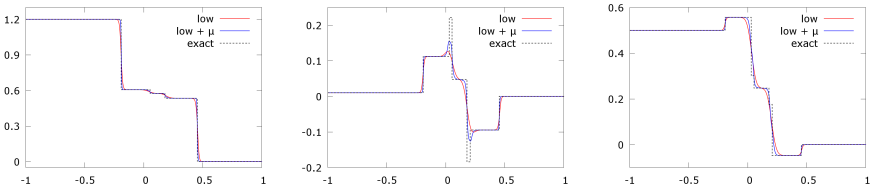

(a) u_x (b) u_y (c) u_z

(d) u_x (e) u_y (f) u_z

Figure 3: Numerical solutions of the Ryu-Jones problem using the viscosity operator (14) and its scaled version "$+\mu$" (20) at $T_{end} = 0.2$ ($h = \frac{1}{512}$)

data

$$(u_z, B_x, B_y, B_z, p) = (0., \frac{2.5}{\sqrt{4\pi}}, 0, 0, 0.5) \tag{60}$$

$$(\rho, \rho u_x, \rho u_y) = \begin{cases} (1,0,0) & \text{if } r > r_1 \\ (10, 100(0.5-y), 100(x-0.5)) & \text{if } r < r_0 \\ (1+9f, 100f(0.5-y), 100f(x-0.5)) & \text{otherwise} \end{cases}, \tag{61}$$

where $r = \sqrt{(x-0.5)^2 + (y-0.5)^2}$, $r_0 = 0.1$, $r_1 = 0.115, \gamma = \frac{5}{3}$ and $f = \frac{r_1 - r}{r_1 - r_0}$. In Fig. 4 the density and the thermal pressure of the numerical solution using the different divergence cleaning approaches from section 3 and the scaled version of the artificial viscosity operator (20) are shown. The solutions look very similar to those of the original rotor problem found in the literature, e.g. [4, 26]. For a better evaluation we compared the FCT solutions with and without the shock detector scaling ('$+\mu$') with the reference solution computed by Athena [25] using a third order method on a grid with 400 cells. The direct comparisons at $x = y$ are shown in Fig. 5. We see that the solutions are smeared out at the peaks but overall there is a good agreement with the profile. Comparing the results of the two divergence cleaning approaches we only have minor differences. The solutions obtained with the μ-scaled viscosity operator are a little bit more accurate. For the potA strategy we obtain $\int_\Omega \nabla \cdot \mathbf{B} \, \mathrm{d}\mathbf{x} = 6.52 \times 10^{-11}$ and $\int_\Omega |\nabla \cdot \mathbf{B}| \, \mathrm{d}\mathbf{x} = 3.75 \times 10^{-1}$ and for the RT strategy we obtain $\int_\Omega \nabla \cdot \mathbf{B} \, \mathrm{d}\mathbf{x} = 4.81 \times 10^{-11}$, $\int_\Omega |\nabla \cdot \mathbf{B}| \, \mathrm{d}\mathbf{x} = 6.12 \times 10^{-1}$ and $\int_\Omega \nabla \cdot \mathbf{B}_{RT} \, \mathrm{d}\mathbf{x} = 8.42 \times 10^{-12}$, $\int_\Omega |\nabla \cdot \mathbf{B}_{RT}| \, \mathrm{d}\mathbf{x} = 1.27 \times 10^{-9}$.

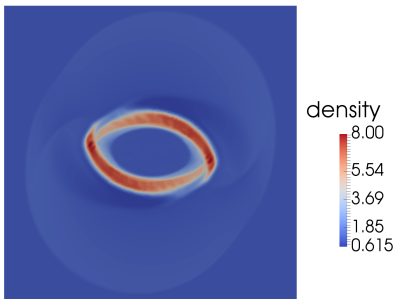

(a) Density ρ - RT

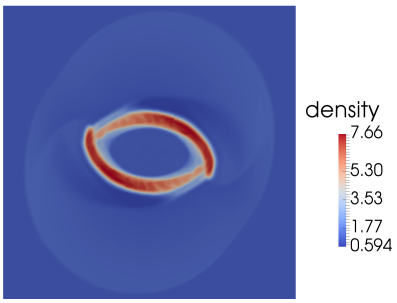

(b) Density ρ - potA

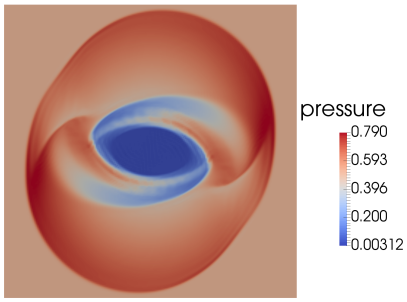

(c) Thermal pressure p - RT

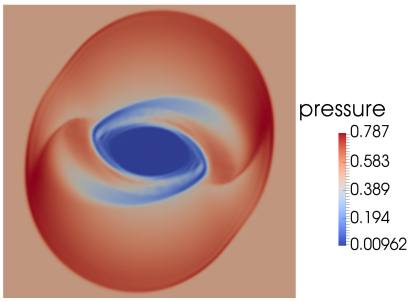

(d) Thermal pressure p - potA

Figure 4: Numerical solutions of the rotor problem at $T_{end} = 0.295$ ($h = \frac{1}{200}$) using different divergences cleaning approaches

4.4. 2d - Orszag-Tang vortex problem

We now consider the Orszag-Tang vortex problem [19] which is another widely used test problem for MHD [26, 22]. The initial data is given by

$$(\rho, u_x, u_z, u_z, B_x, B_y, B_z, p)$$
$$= \left(\frac{25}{36\pi}, -\sin(2\pi y), \sin(2\pi x), 0, -B_0 \sin(2\pi y), B_0 \sin(4\pi x), 0, \frac{5}{12\pi}\right), \quad (62)$$

where $B_0 = \frac{1}{\sqrt{4\pi}}$ and $\gamma = \frac{5}{3}$.

In Fig. 6 the numerical solutions for the density and the pressure are shown. Comparing the RT and the potA approach we see that the RT solutions are a little bit smoother than the potA solutions. As before we compare our results with the reference solution computed by Athena [25] using a third order method on a grid with 400 cells (see Fig. 7). The numerical solutions differ from each other a bit but overall they exhibit the same profile. The solutions obtained with the RT version and with the μ-scaled viscosity

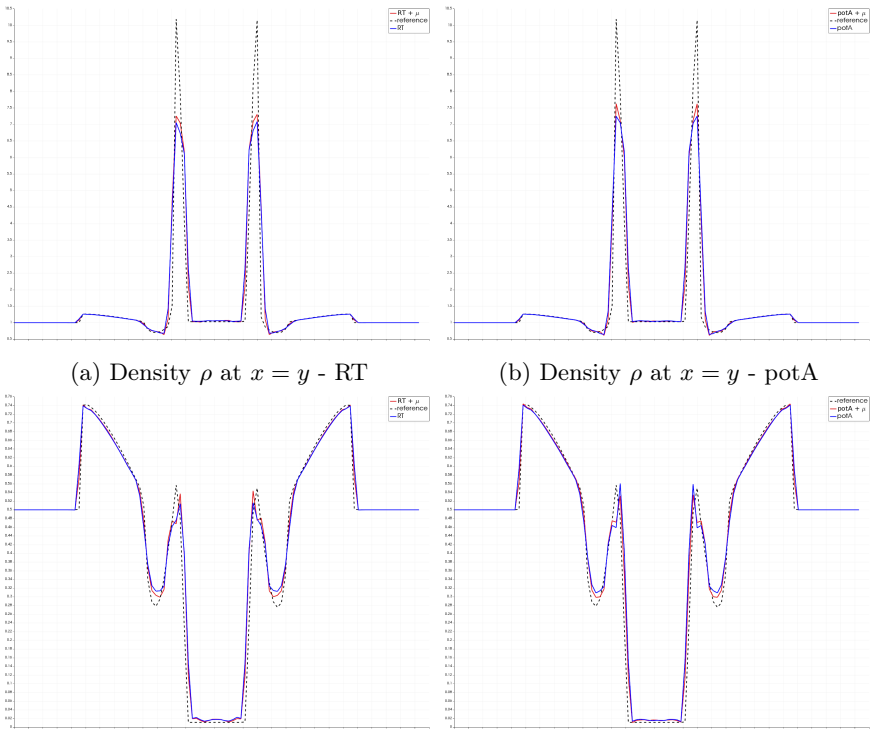

(a) Density ρ at $x = y$ - RT (b) Density ρ at $x = y$ - potA

(c) Thermal pressure p at $x = y$ - RT (d) Thermal pressure p at $x = y$ - potA

Figure 5: Comparison of the numerical solutions of the rotor problem at $T_{end} = 0.295$ ($h = \frac{1}{200}$) using the viscosity operator (14) and its scaled version "$+\mu$" (20)

operator seem to be the most accurate ones. For the potA strategy we obtain $\int_\Omega \nabla \cdot \mathbf{B}\,\mathrm{d}\mathbf{x} = 2.18 \times 10^{-17}$ and $\int_\Omega |\nabla \cdot \mathbf{B}|\,\mathrm{d}\mathbf{x} = 1.24$ and for the RT strategy we obtain $\int_\Omega \nabla \cdot \mathbf{B}\,\mathrm{d}\mathbf{x} = -1.11 \times 10^{-17}$, $\int_\Omega |\nabla \cdot \mathbf{B}|\,\mathrm{d}\mathbf{x} = 1.12$ and $\int_\Omega \nabla \cdot \mathbf{B}_{RT}\,\mathrm{d}\mathbf{x} = -1.25 \times 10^{-17}$, $\int_\Omega |\nabla \cdot \mathbf{B}_{RT}|\,\mathrm{d}\mathbf{x} = 3.60 \times 10^{-2}$.

5. Conclusion

In this paper we extended the FCT scheme for the Euler equations to the MHD equations. We presented a scaled artificial viscosity operator and showed by numerical experiments that this scaling can lead to more accurate solutions than without it. To obtain a divergence-free magnetic field in 2d we presented two predictor-corrector strategies where the FCT solution is used as a predictor. One strategy takes into account the magnetic potential which has to be updated in each time step and the other defines the magnetic field in the Raviart-Thomas FE space. Both strategies lead to similar results whereas the solutions of the second strategy seems to be a bit more accurate. Also from an analytical point

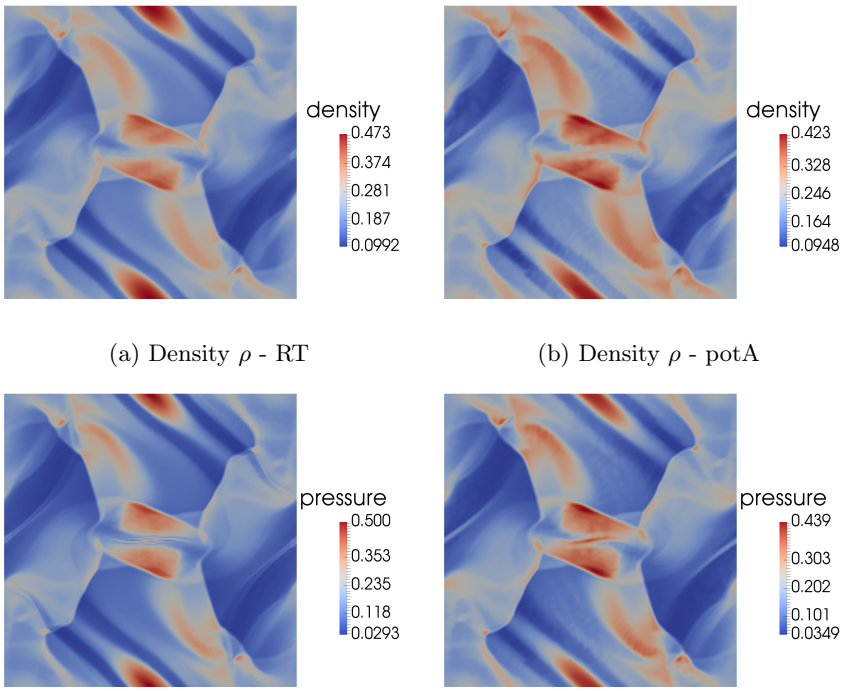

(a) Density ρ - RT

(b) Density ρ - potA

(c) Thermal pressure p - RT

(d) Thermal pressure p - potA

Figure 6: Numerical solutions of the Orszag-Tang vortex problem at $T_{end} = 0.5$ ($h = \frac{1}{200}$) using different divergence cleaning approaches

of view the use of the Raviart-Thomas FE space is reasonable since it provides a discrete version of $H(div)$ which is the right space for the magnetic field. In future work we will study how the limiting strategy of the FCT scheme can be improved since it can resolve contact discontinuities and shocks very well but smears out rotational discontinuities.

Acknowledgements. This research was supported by the German Research Association (DFG) under grant KU 1530/15-2.

[1] J. C. Adam, A. Gourdin Serveniere, J.-C. Nédélec, and P.-A. Raviart. Study of an implicit scheme for integrating Maxwell's equations. *Comput. Methods Appl. Mech. Engrg.*, 22(3):327–346, 1980.

[2] M. Alnæs, J. Blechta, J. Hake, A. Johansson, B. Kehlet, A. Logg, C. Richardson, J. Ring, M. Rognes, and G. Wells. The FEniCS project version 1.5. *Archive of Numerical Software*, 3(100), 2015.

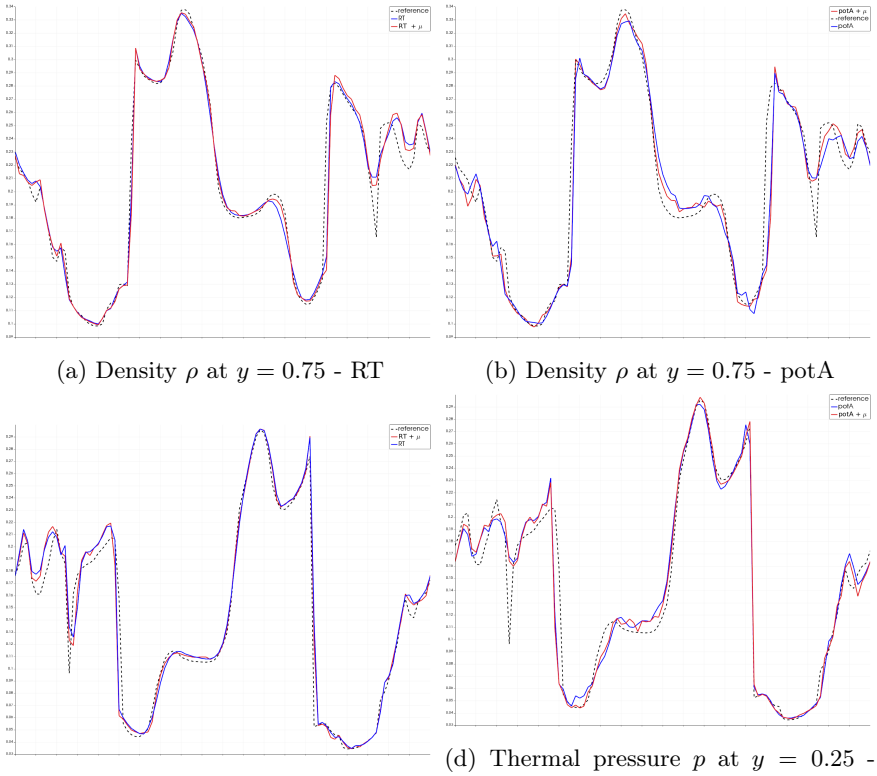

(a) Density ρ at $y = 0.75$ - RT

(b) Density ρ at $y = 0.75$ - potA

(c) Thermal pressure p at $y = 0.25$ - RT

(d) Thermal pressure p at $y = 0.25$ - potA

Figure 7: Comparison of the numerical solutions of the Orszag-Tang vortex problem at $T_{end} = 0.5$ ($h = \frac{1}{200}$) using the viscosity operator (14) and its scaled version "+μ" (20)

[3] S. Badia and J. Bonilla. Monotonicity-preserving finite element schemes based on differentiable nonlinear stabilization. *CoRR*, abs/1606.08743, 2016.

[4] D. S. Balsara and D. S. Spicer. A staggered mesh algorithm using high order Godunov fluxes to ensure solenoidal magnetic fields in magnetohydrodynamic simulations. *J. Comput. Phys.*, 149(2):270–292, 1999.

[5] P. B. Bochev and A. C. Robinson. Matching algorithms with physics: exact sequences of finite element spaces. In *Collected lectures on the preservation of stability under discretization (Fort Collins, CO, 2001)*, pages 145–165. SIAM, Philadelphia, PA, 2002.

[6] D.L. Book, J.P. Boris, and K. Hain. Flux-corrected transport II: Generalizations of the method. *J. Comput. Phys.*, 18(3):248 – 283, 1975.

[7] J. P. Boris and D. L. Book. Flux-corrected transport. I. SHASTA, a fluid

transport algorithm that works [J. Comput. Phys. **11** (1973), no. 1, 38–69]. *J. Comput. Phys.*, 135(2):170–186, 1997. With an introduction by Steven T. Zalesak, Commemoration of the 30th anniversary of J. Comput. Phys.

[8] J. U. Brackbill and D. C. Barnes. The effect of nonzero $\nabla \cdot \mathbf{B}$ on the numerical solution of the magnetohydrodynamic equations. *J. Comput. Phys.*, 35(3):426–430, 1980.

[9] M. Brio and C. C. Wu. An upwind differencing scheme for the equations of ideal magnetohydrodynamics. *J. Comput. Phys.*, 75(2):400–422, 1988.

[10] M. Campos Pinto and E. Sonnendrücker. Compatible Maxwell solvers with particles I: conforming and non-conforming 2D schemes with a strong Ampere law. working paper or preprint, April 2016.

[11] C. R. DeVore. Flux-corrected transport techniques for multidimensional compressible magnetohydrodynamics. *J. Comput. Phys.*, 92(1):142 – 160, 1991.

[12] C.A.J. Fletcher. The group finite element formulation. *Computer Methods in Applied Mechanics and Engineering*, 37(2):225 – 244, 1983.

[13] D. Kuzmin. *Algebraic flux correction I. Scalar conservation laws.* In: D. Kuzmin, R. Löhner, S. Turek (eds) *Flux-Corrected Transport: Principles, Algorithms, and Applications.* Springer, 2012. Second edition.

[14] D. Kuzmin, M. Möller, and M. Gurris. *Algebraic flux correction II. Compressible flow problems.* In: D. Kuzmin, R. Löhner, S. Turek (eds) *Flux-Corrected Transport: Principles, Algorithms, and Applications.* Springer, 2012. Second edition.

[15] D. Kuzmin, M. Möller, J. N. Shadid, and M. Shashkov. Failsafe flux limiting and constrained data projections for equations of gas dynamics. *J. Comput. Phys.*, 229(23):8766–8779, November 2010.

[16] C. Lohmann and D. Kuzmin. Synchronized flux limiting for gas dynamics variables. *J. Comput. Phys.*, 326:973–990, 2016.

[17] R. Löhner, K. Morgan, J. Peraire, and M. Vahdati. Finite element flux-corrected transport (FEM-FCT) for the Euler and Navier-Stokes equations. *International Journal for Numerical Methods in Fluids*, 7(10):1093–1109, 1987.

[18] R. Löhner, K. Morgan, M. Vahdati, J. P. Boris, and D. L. Book. FEM-FCT: combining unstructured grids with high resolution. *Comm. Appl. Numer. Methods*, 4(6):717–729, 1988.

[19] S. A. Orszag and C.-M. Tang. Small-scale structure of two-dimensional magnetohydrodynamic turbulence. *Journal of Fluid Mechanics*, 90:129–143, 1 1979.

[20] A. K. Parrott and M. A. Christie. FCT applied to the 2-d finite element solution of tracer transport by single phase flow in a porous medium. *in K. W.Morton and M. J.Baines (eds), Numerical Methods for Fluid Dynamics, Oxford University Press*, page 609–620, 1986.

[21] K.G. Powell, P.L. Roe, T.J. Linde, T.I. Gombosi, and D.L. De Zeeuwy. A solution-adaptive upwind scheme for ideal magnetohydrodynamics. *J. Comput. Phys.*, 154:284–309, 1999.

[22] J. A. Rossmanith. High-order discontinuous Galerkin finite element methods with globally divergence-free constrained transport for ideal MHD. *ArXiv e-prints*, October 2013. http://arxiv.org/abs/1310.4251.

[23] D. Ryu and T. W. Jones. Numerical magnetohydrodynamics in astrophysics: Algorithm and tests for one-dimensional flow. *Astrophys. J.*, 442(1):228–258, 1995.

[24] G. A. Sod. A survey of several finite difference methods for systems of nonlinear hyperbolic conservation laws. *J. Comput. Phys.*, 27(1):1–31, 1978.

[25] J. M. Stone, T. A. Gardiner, P. Teuben, J. F. Hawley, and J. B. Simon. Athena: A new code for astrophysical mhd. *The Astrophysical Journal Supplement Series*, 178(1):137, 2008.

[26] G. Tóth. The $\nabla \cdot B = 0$ constraint in shock-capturing magnetohydrodynamics codes. *J. Comput. Phys.*, 161(2):605 – 652, 2000.

[27] G. Tóth and D. Odstrčil. Comparison of some flux corrected transport and total variation diminishing numerical schemes for hydrodynamic and magnetohydrodynamic problems. *J. Comput. Phys.*, 128(1):82 – 100, 1996.

[28] S.T. Zalesak. Fully multidimensional flux-corrected transport algorithms for fluids. *J. Comput. Phys.*, 31:335–362, 1979.